universe

MDPI

Article

Magnetic Field Effects on the Structure of Neutron Stars

Harsh Chandrakar [1], Ishfaq Ahmad Rather [2], Prashant Thakur [3], Tarun Kumar Jha [1], Rodrigo Negreiros [4,5,6], Carline Biesdorf [7], Mariana Dutra [7] and Odilon Lourenço [7,*]

1 Department of Physics, BITS-Pilani K. K. Birla Goa Campus, Zuarinagar 403726, Goa, India; p20220023@goa.bits-pilani.ac.in (H.C.); tkjha75@gmail.com (T.K.J.)
2 Institut für Theoretische Physik, Goethe Universität, Max-von-Laue-Str. 1, D-60438 Frankfurt am Main, Germany; rather@itp.uni-frankfurt.de
3 Department of Physics, Yonsei University, Seoul 03722, Republic of Korea; prashantthakur1921@gmail.com
4 Department of Physics, Catholic Institute of Technology, Cambridge, MA 02142, USA; rnegreiros@catholic.tech
5 Department of Physics, Universidade Federal Fluminense, Niteroi 24210-346, RJ, Brazil
6 ICRANet, Piazza della Repubblica 10, I-65122 Pescara, Italy
7 Departamento de Física e Laboratório de Computação Científica Avançada e Modelamento (Lab-CCAM), Instituto Tecnológico de Aeronáutica, DCTA, São José dos Campos 12228-900, SP, Brazil; carline.fsc@gmail.com (C.B.); marianadutrarl@gmail.com (M.D.)
* Correspondence: odilon.ita@gmail.com

Abstract

We investigate the impact of ultrastrong magnetic fields on the structure of neutron stars within a density-dependent relativistic mean-field framework (DDME2). In the first case, we incorporate a magnetic field framework through Landau quantization of charged particles, yielding anisotropic pressure contributions and showing that field-induced stiffening increases stellar radii, maximum masses, and tidal deformabilities. To capture anisotropic stresses and geometric distortions, we employ axisymmetric equilibrium configurations computed with the XNS 4.0 code under the extended conformally flat condition. For magnetic field strengths up to 4.5×10^{17} G, we analyze purely poloidal and toroidal geometries across a representative mass range (1.2–2.0 $M_{\odot}$). Axisymmetric models reveal that purely toroidal fields induce prolate deformations reaching $|\bar{e}| \approx 0.67$ for a 1.2 $M_{\odot}$ star, while purely poloidal fields drive oblate deformations with $\bar{e} \approx 0.24$, both diminishing with increasing stellar mass as greater gravitational binding resists magnetic reshaping. These macroscopic effects, combined with microphysical stiffening, have direct implications for gravitational-wave emission and systematic biases in radius measurements. Our study provides a systematic mapping between magnetic field strength, topology, and dense-matter stiffness, offering constraints relevant to multimessenger observations of magnetized neutron stars.

Keywords: neutron stars; magnetars; strong magnetic fields; equation of state; stellar deformation; gravitational waves

Check for updates

Academic Editor: Nicolas Chamel

Received: 14 March 2026
Revised: 17 April 2026
Accepted: 24 April 2026
Published: 28 April 2026

Copyright: © 2026 by the authors. Licensee MDPI, Basel, Switzerland. This article is an open access article distributed under the terms and conditions of the Creative Commons Attribution (CC BY) license.

1. Introduction

Neutron stars (NSs) are unique astrophysical laboratories where the physics of ultra-dense matter, rapid rotation, and extreme magnetic fields converge. Among them, magnetars exhibit surface magnetic fields of order 10^{15} G, while theoretical estimates suggest that internal fields may reach 10^{17}–10^{18} G [1–5]. Such ultrastrong fields are not merely peripheral features: they fundamentally alter the structure and observable properties of NSs.

Magnetic fields influence NSs in two principal ways. First, they modify the microphysical equation of state (EoS). In strong fields, charged particles such as protons and electrons occupy discrete Landau levels, and the associated magnetic energy density contributes an additional, anisotropic pressure [1]. These effects generally stiffen the EoS, increasing pressure support at a given density and thereby raising the maximum mass and radius relative to non-magnetized stars [2]. Second, magnetic fields break spherical symmetry. The Lorentz force associated with ordered field configurations induces bulk distortions: poloidal fields tend to make stars oblate, while toroidal fields drive prolate shapes [4,6–8]. Such deformations are astrophysically significant, as they can generate continuous gravitational waves from rotating stars with non-zero ellipticity.

Direct measurement of the internal magnetic field remains impossible, necessitating reliance on theoretical estimates. The relativistic virial theorem sets an upper bound for the interior field of approximately 10^{18} G, based on the requirement that the magnetic energy does not exceed the gravitational potential energy [9]. Similarly, solving the Einstein–Maxwell equations limits the central field to a few times 10^{18} G for stable poloidal configurations, with the exact limit depending on the EoS [4,5]. Comparable limits apply to purely toroidal configurations [10]. Because the magnetic field magnitude typically varies by less than one order of magnitude from the surface to the center [10,11], achieving a central field $\geq 10^{17}$ G implies a surface field of at least 10^{16} G. While most magnetar observations infer fields of ~10^{15} G, data from 4U 0142+61 suggests fields on the order of 10^{16} G [12,13]. The scarcity of such extreme objects may result from rapid field decay due to axis misalignment [14,15] or instabilities in stars formed via mergers [16–18]. Theoretically, fields $\geq 10^{15}$ G can be generated by supernova simulations given sufficient angular momentum in the progenitor [19]. The influence of such strong fields on the NS EoS and global properties (mass and radius) has been the subject of extensive prior study [2,10,20–29].

Modeling magnetized NSs requires approaches that balance realism and tractability. A simplified method incorporates magnetic effects into EoS and solves the Tolman–Oppenheimer–Volkoff (TOV) equations under spherical symmetry [30,31]. This captures global changes in mass–radius (M-R) relations and tidal deformability but neglects anisotropic stresses and shape deformations. A more complete treatment solves the coupled Einstein–Maxwell equations in axisymmetry. In this work, we adopt the XNS 4.0 code [8], which implements the extended Conformally Flat Condition (XCFC) to compute equilibrium configurations of magnetized stars. This framework allows us to explore both poloidal and toroidal field geometries and quantify their impact on stellar deformation. This deviation from sphericity is quantified by the mean deformation parameter $\bar{e} = (I_{zz} - I_{xx})/I_{zz}$, where I_{zz} and I_{xx} are the moments of inertia about the $z-$ and $x-$axes, respectively [32]. A positive value of $\bar{e}$ corresponds to an oblate shape, while a negative value indicates a prolate shape.

We employ the DDME2 EoS [33], a density-dependent relativistic mean-field model calibrated to nuclear data and capable of supporting two-solar-mass NSs. Using this baseline, we construct equilibrium models across a representative mass range (1.2–2.0 $M_\odot$) and apply magnetic fields up to 10^{17} G. Our analysis combines spherical TOV calculations with axisymmetric `XNS` simulations to assess how density-dependent magnetic fields influence stellar radii, maximum masses, tidal deformability, and quadrupole ellipticity. These results provide a systematic mapping between magnetic field strength, field geometry, and dense-matter stiffness, with direct implications for multimessenger observations of NSs [34–39].

While pioneering works such as [7,8,10] established the foundations of magnetized NS modeling, they typically focused on fixed magnetic field configurations or idealized geometries without explicitly incorporating density-dependent field profiles into the EoS.

In contrast, our study combines a density-dependent magnetic field parameterization with both spherical (TOV) and axisymmetric (XNS) approaches. This dual framework allows us to capture not only the global stiffening of the EoS and its impact on mass–radius relations but also the geometric deformations induced by poloidal and toroidal fields. By systematically comparing these effects across a range of stellar masses, our work provides a more comprehensive mapping between magnetic field strength, field topology, and observable NS properties. Several interesting works on the NS EoS with the strong magnetic field can be found in refs. [27,40–50].

Beyond the microphysical stiffening of the EoS, the macroscopic deformations induced by the strong magnetic fields have profound consequences for multi-messenger astrophysics. The geometric distortion of the NS, quantified by the mean deformation parameter $\bar{e}$, serves as a direct link between the internal magnetic topology and observable signals. Specifically, the distinction between prolate deformations ($\bar{e} < 0$), driven by toroidal fields, and oblate deformations ($\bar{e} > 0$), driven by poloidal fields, dictates the nature of gravitational wave emission and the interpretation of electromagnetic light curves. While current observational constraints on the dense matter EoS rely heavily on the assumption of spherical symmetry or purely rotational flattening, the presence of internal fields exceeding 10^{16}–10^{17} G introduces a degeneracy. The resulting magnetic "mountains" can sustain continuous gravitational wave emission detectable by next-generation interferometers, while simultaneously introducing systematic biases in radius measurements derived from X-ray pulse profile modeling. Quantifying these deformations is therefore essential not only for understanding magnetar structure but also for the robust interpretation of data from current and future observational facilities.

The paper is organized as follows. Section 2 outlines the theoretical framework, including the DDME2 EoS and the magnetic field parameterization. Section 3 presents results from spherical TOV calculations, highlighting how magnetic stiffening of the EoS modifies the M-R relations and tidal deformability. Section 4 introduces axisymmetric models computed with the XNS 4.0 solver, where we analyze the impact of the poloidal and toroidal field geometries on stellar deformation. Section 5 discusses the astrophysical implications of these "giant" magnetic deformations, focusing on their role in continuous gravitational-wave emission and systematic biases in X-ray pulse profile modeling. Finally, Section 6 summarizes our conclusions and identifies directions for future work.

2. Methodology

In the relativistic mean-field (RMF) framework, nuclear matter is described through interactions among baryons mediated by meson exchange. The relevant mesonic fields include the scalar-isoscalar σ, the vector-isoscalar ω, and the vector-isovector ρ. The total Lagrangian density contains contributions from baryons, leptons, mesons, and their interactions. Within the density-dependent RMF (DD-RMF) approach [51], the meson–baryon coupling constants depend explicitly on the baryon density.

The DD-RMF Lagrangian density can be written as [52]

$$\begin{aligned}\mathcal{L}_m = &\sum_B \bar{\psi}_B \left\{ \gamma_\mu \left(iD^\mu - g_\omega(\rho_B)\omega_\mu - \frac{1}{2} g_\rho(\rho_B)\rho_\mu \tau \right) - \left(M - g_\sigma(\rho_B)\sigma \right) \right\} \psi_B \\ &+ \frac{1}{2}\left(\partial^\mu \sigma \partial_\mu \sigma - m_\sigma^2 \sigma^2 \right) - \frac{1}{4} W^{\mu\nu} W_{\mu\nu} + \frac{1}{2} m_\omega^2 \omega_\mu \omega^\mu - \frac{1}{4} R^{\mu\nu} R_{\mu\nu} + \frac{1}{2} m_\rho^2 \rho_\mu \rho^\mu \\ &+ \sum_l \bar{\psi}_l (i\gamma_\mu D^\mu - m_l)\psi_l, \end{aligned} \tag{1}$$

where B sums over the baryons (n, p) and l over the leptons (e^-, μ^-). ψ_B and ψ_l represent the baryonic and leptonic Dirac fields, respectively. The mesonic tensor fields and covariant derivative are defined as

$$\begin{aligned} W^{\mu\nu} &= \partial^\mu W^\nu - \partial^\nu W^\mu, \\ R^{\mu\nu} &= \partial^\mu R^\nu - \partial^\nu R^\mu, \\ D^\mu &= \partial^\mu + eQA^\mu. \end{aligned} \tag{2}$$

The electromagnetic contribution to the Lagrangian density is given by

$$\mathcal{L}_f = -\frac{1}{16\pi} F_{\mu\nu} F^{\mu\nu}, \tag{3}$$

where $F_{\mu\nu} = \partial_\mu A_\nu - \partial_\nu A_\mu$. The complete Lagrangian density in the presence of a magnetic field is then

$$\mathcal{L} = \mathcal{L}_m + \mathcal{L}_f. \tag{4}$$

In the DD-RMF model, the density dependence of the coupling constants is introduced through

$$g_{iB}(\rho_B) = g_{iB}(\rho_0) f_i(x), \tag{5}$$

for $i = \sigma, \omega$, where $x = \rho_B/\rho_0$ and ρ_0 denotes the saturation density. The function $f_i(x)$ is parametrized as

$$f_i(x) = a_i \frac{1 + b_i(x + d_i)^2}{1 + c_i(x + d_i)^2}. \tag{6}$$

For the ρ meson, the coupling takes the form

$$g_\rho(\rho_B) = g_\rho(\rho_0) exp[-a_\rho(x - 1)]. \tag{7}$$

The parametrization initially involves eight parameters, which are reduced to three using constraint conditions from refs. [53–55] to reproduce nuclear matter properties. We adopt the DDME2 parameter set [33].

The energy density and pressure in a magnetic field are obtained from the energy–momentum tensor [56,57].

$$T^{\mu\nu} = T^{\mu\nu}_m + T^{\mu\nu}_l, \tag{8}$$

with

$$\begin{aligned} T^{\mu\nu}_m &= \mathcal{E}_m u^\mu u^\nu - P(g^{\mu\nu} - u^\mu u^\nu) + \mathcal{M}B\left(g^{\mu\nu} - u^\mu u^\nu + \frac{B^\mu B^\nu}{B^2}\right), \\ T^{\mu\nu}_l &= \frac{B^2}{4\pi}\left(u^\mu u^\nu - \frac{1}{2} g^{\mu\nu}\right) - \frac{B^\mu B^\nu}{4\pi}. \end{aligned} \tag{9}$$

Here, $\mathcal{M}$ denotes the magnetization per unit volume, and $B^\mu B_\mu = -B^2$. In the presence of a strong magnetic field, the motion of charged baryons and leptons in the plane perpendicular to the field becomes quantized, resulting in discrete single-particle energy levels.

For a uniform magnetic field directed along the z-axis, $B = B\hat{z}$, the energy of a charged particle is given by

$$E_{cb} = \sqrt{k_z^2 + M^{*2} + 2\nu|q|B}, \tag{10}$$

The quantity $\nu = \left(n + \frac{1}{2} - \frac{1}{2}\frac{q}{|q|}\sigma_z\right) = 0, 1, 2, \ldots$ indicates the Landau levels of fermions with electric charge q. n is the orbital angular momentum quantum number and σ_z is the

Pauli matrix. The Fermi momentum of all charged baryons $k_{F,\nu}^{cb}$ and leptons $k_{F,\nu}^{l}$ with Fermi energies E_F^{cb} and E_F^{l}, respectively, are given as [2]

$$k_{F,\nu}^{cb} = \sqrt{(E_F^{cb})^2 - M_{cb}^{*2} - 2\nu|q_{cb}|B},$$
$$k_{F,\nu}^{l} = \sqrt{(E_F^{l})^2 - m_l^2 - 2\nu|q_l|B}. \tag{11}$$

The maximum Landau level ν is determined by the requirement that the corresponding Fermi momentum remains real and non-negative for each particle.

$$\nu_{max} = \left[\frac{(E_F^{cb})^2 - M_{cb}^{*2}}{2|q_{cb}|B}\right],$$
$$\nu_{max} = \left[\frac{(E_F^{l})^2 - m_l^2}{2|q_l|B}\right], \tag{12}$$

for charged baryons and leptons, respectively.

From Equation (9), we get the total energy density as

$$\mathcal{E} = \mathcal{E}_m + \frac{B^2}{8\pi}. \tag{13}$$

The expression for the matter energy density $\mathcal{E}_m$ obtained in the presence of a magnetic field can be found in Ref. [49].

The total pressure can be expressed in components perpendicular and parallel to the local magnetic field as

$$P_\perp = P_m - \mathcal{M}B + \frac{B^2}{8\pi},$$
$$P_\parallel = P_m - \frac{B^2}{8\pi}, \tag{14}$$

where the magnetization is given by

$$\mathcal{M} = \partial P_m / \partial B. \tag{15}$$

The microphysical framework developed above provides the magnetized EoS that determines the internal pressure and energy density of NS matter. It is important to clarify the nature of the pressure anisotropy presented here. Following ref. [58], the kinetic matter pressure P_m remains isotropic in the local fluid frame. The components $P_\perp$ and $P_{||}$ represent the effective pressures derived from the total energy–momentum tensor, where the magnetic Maxwell stress provides the directional dependence. This distinction ensures that the microphysical stiffening is correctly attributed to the field's contribution to the total stress–energy tensor.

We also extend our analysis to fully self-consistent axisymmetric equilibrium configurations. We model the equilibrium of static, axisymmetric, and strongly magnetized NSs in general relativity using the numerical solver `XNS 4.0` [8,59]. The code employs the extended conformally flat condition (XCFC), a computationally efficient approximation that reduces Einstein's equations to a set of elliptic PDEs for the metric potentials, the lapse function α and the conformal factor ψ [8,60].

Under ideal magnetohydrodynamic (MHD) conditions, when a poloidal magnetic field is present, the magnetic field structure is governed by a formulation based on the Grad–Shafranov (GS) equation. For the toroidal configuration, it is more convenient to prescribe the toroidal component of the vector potential. The solution depends on two

chosen functions, the magnetization $\mathcal{M}(A_\phi)$ and the current function $\mathcal{I}(A_\phi)$, which define the field geometry. The matter distribution is linked to the magnetic field via the relativistic Bernoulli integral.

The toroidal magnetic field component is then specified via a current function $\mathcal{I}(G)$ as $B_\phi = \varpi^{-1}\mathcal{I}(G)$, where $\mathcal{I}(G)$ is

$$\mathcal{I}(G) = K_m G^m, \tag{16}$$

$$\mathcal{M}(G) = -\frac{mK_m^2}{2m-1} G^{2m-1} \tag{17}$$

The parameters K_m and $m \geq 1$ are the toroidal magnetization constant and index. In our analysis, we have used the magnetization index, $m = 1$. Using this prescription, we construct equilibrium models for NS with fixed gravitational masses of 1.2, 1.4, 1.8, and 2.0 $M_\odot$. This selection allows us to investigate a range of stellar configurations, from low-mass to near-maximum-mass objects, and how the global stellar properties are affected by the strong magnetic field.

For configurations with a poloidal magnetic field mixed-field geometries, the `XNS` code prescribes the field structure via the magnetization function $\mathcal{M}(A_\phi)$ and the electric current function $\mathcal{I}(A_\phi)$, following the formalism of [61]:

$$\mathcal{M}(A_\phi) = k_{\rm pol}\left(A_\phi + \frac{1}{2}\xi A_\phi^2\right), \tag{18}$$

$$\mathcal{I}(A_\phi) = \frac{a}{\zeta+1}\,\Theta[A_\phi - A_\phi^{\rm max}]\left(A_\phi - A_\phi^{\rm max}\right)^{\zeta+1}. \tag{19}$$

Here, $k_{\rm pol}$ and a are strength parameters for the poloidal and toroidal components, respectively, while ξ and ζ introduce non-linearities. The Heaviside function, $\Theta[\cdot]$, ensures that the toroidal currents are confined within the star.

To provide a clear baseline for the effects of magnetic topology, this study is restricted to the linear regime by setting the non-linearity parameters to $\xi = 0$ and $\zeta = 0$. Within this linear framework, we construct two classes of models: purely poloidal ($a = 0$) and mixed-field ($a > 0$). For each class, solutions are generated for fixed gravitational masses of 1.2, 1.4, 1.8, and 2.0 $M_\odot$, enabling a systematic analysis of the interplay between magnetic topology and stellar compactness.

3. Spherical Baseline Models—TOV Results

We analyze four figures illustrating the properties of magnetized NSs within the framework of the DDME2 EoS [33]. The results reveal a clear causal link between the inclusion of a density-dependent magnetic field and the star's macroscopic properties. To isolate the impact of Landau quantization on the EoS independently of macroscopic shape changes, we employ a spherically symmetric baseline using the chaotic magnetic field approximation [62,63]. In this framework, the magnetic field is assumed to be randomly oriented on small scales, ensuring that $\nabla \cdot \vec{B} = 0$ is satisfied on average and that the magnetic contribution to the energy–momentum tensor becomes effectively isotropic.

The maximum possible influence of ultra-strong magnetic fields on NS structure is then assessed by solving the TOV equations under spherical symmetry. In this benchmark, the perpendicular pressure component $P_\perp$, which provides the stiffest contribution, is adopted as the isotropic input. This choice establishes an upper theoretical bound on the enhancement of stellar mass, radius, and tidal deformability driven purely by EoS-level Landau quantization.

The local pressure components $P_\perp$ and $P_\parallel$, derived in Equations (14) and (15), include a $B^2/8\pi$ term for a directed field. In contrast, the chaotic approximation assumes small-scale, randomly oriented domains, such that the magnetic stress–energy tensor is averaged and the magnetic pressure becomes effectively isotropic, $P_{\rm mag} = B^2/24\pi$. This treatment enables a consistent one-dimensional analysis while providing a quantitative upper bound on EoS-level effects.

Spherical symmetry is maintained here to establish a microphysical baseline. If the parallel component $P_\parallel$ were adopted instead, the resulting EoS would be significantly softer, leading to lower maximum masses. These spherical results serve as a reference for comparison with the axisymmetric models presented in Section 4, which incorporate geometric flattening. The results are interpreted within the context of the TOV equations for relativistic stellar structure [30,31].

3.1. The Magnetic Field Profile

The magnetic field profile adopted in this study follows the parameterization introduced in [11] and subsequently employed in several works [49,50,64]. This model expresses the magnetic field strength as a function of the local thermodynamic properties of stellar matter, specifically the baryon chemical potential, μ_B. The profile is further connected to the global magnetic dipole moment of the star, μ.

The functional form of the magnetic field is given by

$$B^*(\mu_B) = \frac{\left(a + b\mu_B + c\mu_B^2\right)}{B_c^2}\mu, \tag{20}$$

where μ_B denotes the baryon chemical potential (in MeV), and μ represents the dipole magnetic moment (in units of Am^2), such that B^* is expressed in terms of the electron critical field $B_c = 4.414 \times 10^{13}$ G. The coefficients a, b, and c are taken as $a = -0.0769$ G^2/(Am^2), $b = 1.20 \times 10^{-3}$ G^2/(Am^2 MeV), and $c = -3.46 \times 10^{-7}$ G^2/(Am^2 MeV^2). These values are obtained from a fit to the magnetic field profile along the polar direction of an NS with a baryonic mass of 2.2 $M_\odot$.

The functional form of the magnetic field in Equation (20) is physically motivated by the results of [11], where self-consistent solutions of the coupled Einstein–Maxwell equations were used to map the internal field distribution of magnetars. Unlike common exponential prescriptions that are often ad-hoc, this quadratic dependence on the baryon chemical potential μ_B reflects the polynomial field increase toward the stellar center found in realistic general-relativistic models. By employing a profile derived from macroscopic current distributions, we ensure that the microphysical EoS stiffening is consistent with the field gradients supported by numerical relativity simulations. This approach also mitigates the risk of Maxwell equation violations often found in purely density-dependent exponential models [65].

This parameterization provides a computationally efficient way to incorporate a magnetic field that depends on local matter conditions into the EoS, while ensuring that the integrated field corresponds to a chosen global magnetic dipole moment μ.

Since the baryon chemical potential μ_B is a monotonically increasing function of baryon density ρ_B, this model produces a magnetic field that grows with density, as illustrated in the left panel of Figure 1. This ensures that the magnetic field is strongest in the high-density core of the NS and weakest in the low-density crust. For the largest dipole moment considered, $\mu = 10^{32}$ Am^2, the central magnetic field (at typical central densities of $\rho_c \approx 1.2\,\mathrm{fm}^{-3}$) reaches a magnetar-strength value of $B_c \approx 4.5 \times 10^{17}$ G. The surface field is slightly lower, $B \approx 1.15 \times 10^{17}$ G.

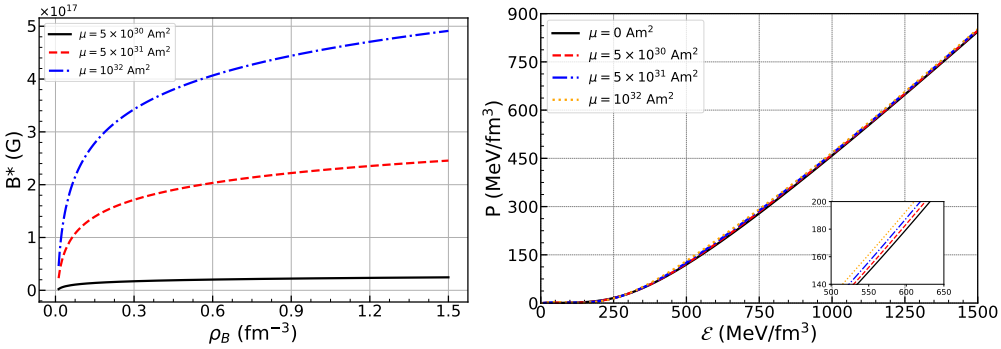

Figure 1. (**Left panel**): The density-dependent magnetic field profile, showing the magnetic field strength B^* as a function of baryonic number density ρ_B for three different values of the magnetic dipole moment μ. (**Right panel**): The corresponding Equation of State (EoS), plotting total pressure P versus total energy density $\mathcal{E}$.

The magnetic field contributes to the total energy–momentum tensor of the stellar fluid. In the isotropic approximation, this contribution appears as an additional magnetic pressure term, $P_{\rm mag}$, proportional to the square of the field strength, $P_{\rm mag} \propto B^2$. Since the magnetic field B depends on the local chemical potential—and therefore on the density—the magnetic pressure inherits this dependence as well.

We acknowledge that utilizing a fitted functional form as a local prescription entails certain limitations. While the coefficients (a, b, c) are calibrated to a representative 2.2 $M_\odot$ star to establish a robust EoS benchmark [11], they do not constitute an exact global solution for every possible stellar mass or topology. In a strictly self-consistent model, the magnetic field and the matter distribution must be solved simultaneously via the Grad–Shafranov equation. However, for the purposes of isolating EoS-level effects in the spherical baseline (Section 3), this parameterization provides a necessary and physically grounded approximation that bridges the gap between microscopic Landau quantization and macroscopic magnetic stress. The right panel of Figure 1 shows the total pressure, P, as a function of the total energy density, $\mathcal{E}$, for the baseline DDME2 EoS ($\mu = 0$) and three magnetized cases. Here, we explicitly define the pressure as the perpendicular component, acting orthogonally to the magnetic field lines, which includes the magnetic pressure contribution. The plot demonstrates that, for any given energy density, the pressure increases systematically with larger magnetic dipole moments, μ, indicating that the EoS stiffens as the magnetic field strength grows. This additional magnetic pressure enhances the matter's resistance to compression.

The stiffening of the EoS at the microscopic level has direct and observable consequences for the macroscopic structure of the NS, which is determined by solving the equations of general relativistic hydrostatic equilibrium.

3.2. The Mass–Radius Relation

The mass–radius (M-R) relation for a given EoS is obtained by integrating the TOV equations. The left panel of Figure 2 shows the M-R curves corresponding to the four EoSs from the right panel of Figure 1.

The results show a clear trend: as the magnetic field strength increases, the mass–radius (M-R) curve shifts toward larger radii and higher maximum masses. This behavior is a direct consequence of the stiffening of the EoS. A stiffer EoS provides a stronger pressure gradient to counteract the inward pull of gravity, thereby supporting a larger radius for a given mass and a greater overall mass before gravitational collapse. For the non-magnetized case ($\mu = 0$), the DDME2 EoS yields a maximum mass of $M_{\rm max} \approx 2.48\, M_\odot$. As shown in the left panel of Figure 2, the most strongly magnetized DDME2 model ($\mu = 10^{32}$ Am^2)

reaches a maximum mass of $M_{max} \approx 2.69\ M_\odot$. While this value falls within the mass range inferred for the secondary component of GW190814 (2.50–2.67 $M_\odot$), we emphasize that the nature of that object remains a subject of intense debate. Our results suggest that magnetic stiffening of the EoS provides a potential theoretical pathway for an NS to exist within the lower mass gap, assuming the presence of internal fields $\geq 10^{17}$ G. However, without a definitive identification of the object or a detailed dynamical stability analysis of such high-mass configurations, this remains a speculative candidate.

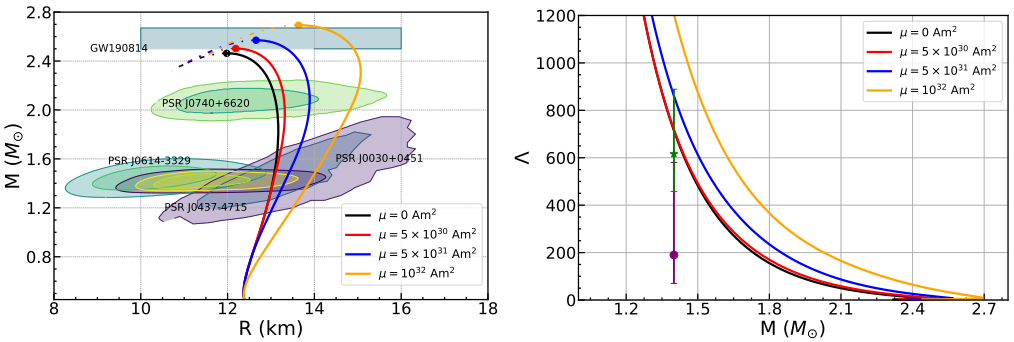

Figure 2. (**Left panel**): The mass–radius (M-R) relation for the magnetized DDME2 EoS. The stiffening of the EoS leads to stellar models with larger radii and higher maximum masses as the magnetic dipole moment μ increases. Observational constraints from several pulsars are shown for comparison [37–39,66–71]. (**Right panel**): The dimensionless tidal deformability Λ as a function of stellar mass M. The observational constraints on Λ from GW170817 and GW190814 are also shown [34,37].

Similarly, the radius of a canonical 1.4 $M_\odot$ NS increases from approximately 13.03 km to 13.89 km, an increase of about 6%. All calculated curves remain consistent with current observational constraints from pulsars such as PSR J0740+6620 [69,70]. It is worth noting that by employing the perpendicular pressure component ($P_\perp$), which exceeds the parallel component, these spherical models effectively place an upper bound on the maximum stellar mass, as they do not account for the geometric flattening that would naturally relieve anisotropic stress.

During the inspiral of a binary NS system, each star is tidally deformed by its companion. The dimensionless tidal deformability, Λ, quantifies this response and is extremely sensitive to the stellar radius, scaling as $\Lambda \propto (R/M)^5$ for a fixed mass M. A larger, less compact star is more easily deformed, resulting in a larger value of Λ [72,73].

The right panel of Figure 2 presents the tidal deformability, Λ, as a function of stellar mass, M. As expected from the M-R relation, Λ increases significantly with magnetic field strength for any given mass. For a 1.4 $M_\odot$ NS, $\Lambda_{1.4}$ rises from ≈715 in the non-magnetized case to ≈860 for $\mu = 5 \times 10^{31}$ Am^2, representing an increase of over 13%. This magnitude is consistent with theoretical predictions that magnetar-strength fields can enhance Λ by 4–18%. These results highlight the importance of accounting for magnetic fields when interpreting gravitational-wave data, such as GW170817 or GW190814, to constrain the dense matter EoS. None of the EoSs satisfy the tidal deformability limit inferred from GW170817, but they do satisfy the limit from GW190814 if the secondary component is assumed to be a supermassive NS, as discussed in several studies. For $\mu = 10^{32}$ Am^2, the tidal deformability increases further to ≈1200.

It is critical to note that the same magnetic stiffening that supports high masses also leads to an increase in the dimensionless tidal deformability. For our models with $\mu \geq 5 \times 10^{31}$ Am^2, the canonical tidal deformability ($\Lambda_{1.4} \approx$ 860–1200) exceeds the upper limit of 800 established by the GW170817 event at 90% confidence [34]. This tension implies that if the secondary component of GW190814 is indeed a magnetized NS, it must

belong to a distinct population—perhaps characterized by different formation histories or higher initial magnetic flux—that does not share the same EoS constraints as the more compact binary components observed in GW170817. We note that these results rely on the standard TOV equations, which assume a spherically symmetric spacetime. It must be emphasized that the spherical results presented here serve only to quantify EoS-driven stiffening and remain internally inconsistent for central fields $\geq 10^{17}$ G. Consequently, the mass expansions reported in this section represent theoretical extrema. However, strong magnetic fields break this symmetry. A fully self-consistent treatment requires solving the Einstein–Maxwell equations for distorted spacetimes using advanced numerical libraries, such as LORENE [4,9,49,50,74]. While a full spectral analysis using LORENE is beyond the scope of this work, the spherical approximation used here serves a specific purpose. It isolates the microphysical stiffening of the EoS (due to Landau quantization and magnetic pressure) from the macroscopic geometric deformations. This allows us to estimate the mass enhancement driven purely by the EoS. To resolve this inconsistency and account for the realistic oblate or prolate distortions induced by magnetic stresses, we move to a self-consistent axisymmetric framework. We address the geometric deformation effects separately in the following section using the `XNS` code.

4. Axisymmetric Magnetized Models—XNS Results

Building upon the microphysical benchmarks from Section 3, the XNS 4.0 solver is employed to model the equilibrium of static, axisymmetric NSs. In contrast to the spherical baseline, this framework accounts for the anisotropic stresses that generate macroscopic geometric distortions. Earlier studies primarily utilized idealized polytropic equations of state within the XNS solver; here, the DDME2 density-dependent relativistic mean-field model is integrated [8]. This approach enables a self-consistent mapping of how the underlying nuclear matter properties—specifically the density-dependent meson–baryon couplings—interact with magnetic-field-induced geometric distortions.

We construct a series of equilibrium models for non-rotating, magnetized NSs using the XNS 4.0 code. Our analysis is divided into two primary cases based on the magnetic field geometry: a purely toroidal configuration and a purely poloidal configuration, each with a fixed maximum magnetic field strength of $B_{\max} = 4.5 \times 10^{17}$ G. The purely poloidal and purely toroidal magnetic field configurations are known to be dynamically unstable on Alfvén timescales and are expected to evolve toward mixed-field equilibria [75]. In this work, these configurations are considered limiting cases to isolate the effects of magnetic topology. The magnetic field configurations adopted here do not arise from a fully self-consistent physical evolution of the system [76]. In realistic NSs, processes such as Hall drift, ambipolar diffusion, and magnetic field dissipation can modify the field structure and strength over time. The present results should therefore be interpreted as equilibrium configurations rather than fully self-consistent evolutionary models.

In this study, the effects of stellar rotation are explicitly neglected in order to isolate the influence of magnetic fields on stellar structure. Including rotation would introduce additional, competing deformation mechanisms, such as centrifugal forces, which are beyond the scope of the present work and are left for future investigations. We then explore how the global properties of the NSs vary across gravitational masses of 1.2, 1.4, 1.8, and 2.0 $M_\odot$.

4.1. Purely Toroidal Magnetic Field Configuration

The global physical quantities for the equilibrium models with a purely toroidal magnetic field are summarized in Table 1. As the gravitational mass (M) increases from 1.2 $M_\odot$ to 2.0 $M_\odot$, the central density (ρ_c) rises from 5.270×10^{14} g/cm^3 to 6.999×10^{14} g/cm^3. This

indicates that more massive stars are more compact, requiring higher central densities to support themselves against gravitational collapse. Correspondingly, the equatorial radius (r_e) decreases across the sequence (13.069, 12.173, 11.210, and 10.830 km), as does the circumferential radius ($R_{\rm circ}$) (14.806, 14.241, 13.956, and 13.918 km) for the 1.2, 1.4, 1.8, and 2.0 $M_\odot$ models, respectively. Here, r_e and r_p denote the equatorial and polar radii, which are coordinate distances to the stellar surface, while $R_{\rm circ}$ is the circumferential radius, defined from the proper equatorial circumference ($R_{\rm circ} = C/2\pi$). Unlike r_e and r_p, $R_{\rm circ}$ is a coordinate-independent, physical measure of the NS radius in general relativity.

Table 1. Global physical quantities of the equilibrium models with maximum magnetic field strength in the purely toroidal case ($B_{\rm max} = 4.5 \times 10^{17}$ G). Here, ρ_c denotes the central baryon density, M the gravitational mass, m_b the baryonic mass, r_e the equatorial radius, r_p the polar radius, $R_{\rm circ}$ the circumferential radius, $\bar{e}$ the deformation parameter, Φ the magnetic flux.

M ($M_\odot$)	ρ_c (10^{14} g/cm^3)	m_b ($M_\odot$)	r_e (km)	r_p/r_e	$R_{\rm circ}$ (km)	$\bar{e}$ (10^{-1})	Φ (10^{21} Wb)
1.2	5.270	1.306	13.069	1.171	14.806	−6.69	8.411
1.4	5.651	1.556	12.173	1.128	14.241	−4.36	8.181
1.8	6.489	2.086	11.210	1.079	13.956	−2.31	8.308
2.0	6.999	2.368	10.830	1.064	13.918	−1.81	8.587

A strong toroidal magnetic field fundamentally alters the geometry of the star. The toroidal field lines, which wrap around the symmetry axis and exert inward pressure along the equatorial plane, elongate the star into a prolate shape. This is confirmed by a polar-to-equatorial radius ratio (r_p/r_e) greater than unity in all models. The deformation parameter, defined as $\bar{e} = (I_{zz} - I_{xx})/I_{xx}$, where I_{zz} and I_{xx} are the moments of inertia about the z- and x-axes, quantifies this effect and reveals a clear dependence on stellar compactness and self-gravity. The least massive and least dense 1.2 $M_\odot$ star ($\rho_c = 5.270 \times 10^{14}$ g/cm^3) is the most distorted, with $\bar{e} = -6.69 \times 10^{-1}$. As the mass and central density increase, the star becomes more gravitationally bound and resistant to deformation: the 1.4 $M_\odot$ star ($\rho_c = 5.651 \times 10^{14}$ g/cm^3) has a smaller deformation of $\bar{e} = -4.36 \times 10^{-1}$, followed by the 1.8 $M_\odot$ star ($\rho_c = 6.489 \times 10^{14}$ g/cm^3) with $\bar{e} = -2.31 \times 10^{-1}$. Finally, the most massive and densest 2.0 $M_\odot$ model ($\rho_c = 6.999 \times 10^{14}$ g/cm^3) is the closest to spherical, with the smallest deformation of $\bar{e} = -1.81 \times 10^{-1}$.

These structural characteristics are illustrated in Figure 3, which shows the magnetic field strength distribution in the meridional plane for each of the four models. In each panel, the cyan solid lines mark the stellar surface of the magnetized configurations, while the white dashed lines correspond to the unmagnetized counterparts of the same gravitational mass. The prolate deformation is evident from the elongation of the stellar surface along the z-axis. This effect is most pronounced in the 1.2 $M_\odot$ model (panel a) and progressively diminishes with increasing mass, with the 2.0 $M_\odot$ star (panel d) appearing nearly spherical.

To further investigate these effects, we construct sequences of models at fixed gravitational mass while varying the magnetic field strength. The results are shown in Figure 4, which illustrates the variation of global quantities relative to their non-magnetized counterparts along equilibrium sequences at fixed mass. The plots display the changes in central density ($\Delta\rho_c$), circumferential radius ($\Delta R_{\rm circ}$), and mean deformation ($\bar{e}$) as functions of the maximum magnetic field strength, $B_{\rm max}$.

The top-left panel shows that, for a given gravitational mass, the central density increases as the magnetic field strength grows. This occurs because the toroidal magnetic field generates a strong magnetic tension directed inward toward the symmetry axis. This tension compresses the stellar core, requiring higher central densities to maintain hydrostatic equilibrium. Effectively, this magnetic tension acts in concert with gravity,

forcing the stellar matter to pack more densely at the core to generate the necessary balancing outward fluid pressure. Despite this central compression, the overall stellar size expands, as seen in the top-right panel, where the circumferential radius increases with $B_{\max}$. The bottom panel displays the magnitude of the prolate deformation, which grows non-linearly with magnetic field strength. Across all three panels, a consistent trend emerges: structural changes are most pronounced in the least massive stars. For any given $B_{\max}$, the 1.2 $M_{\odot}$ model exhibits the largest increase in density and radius, along with the strongest deformation. This confirms that less massive, and therefore less gravitationally bound, NSs are more susceptible to the influence of strong magnetic fields.

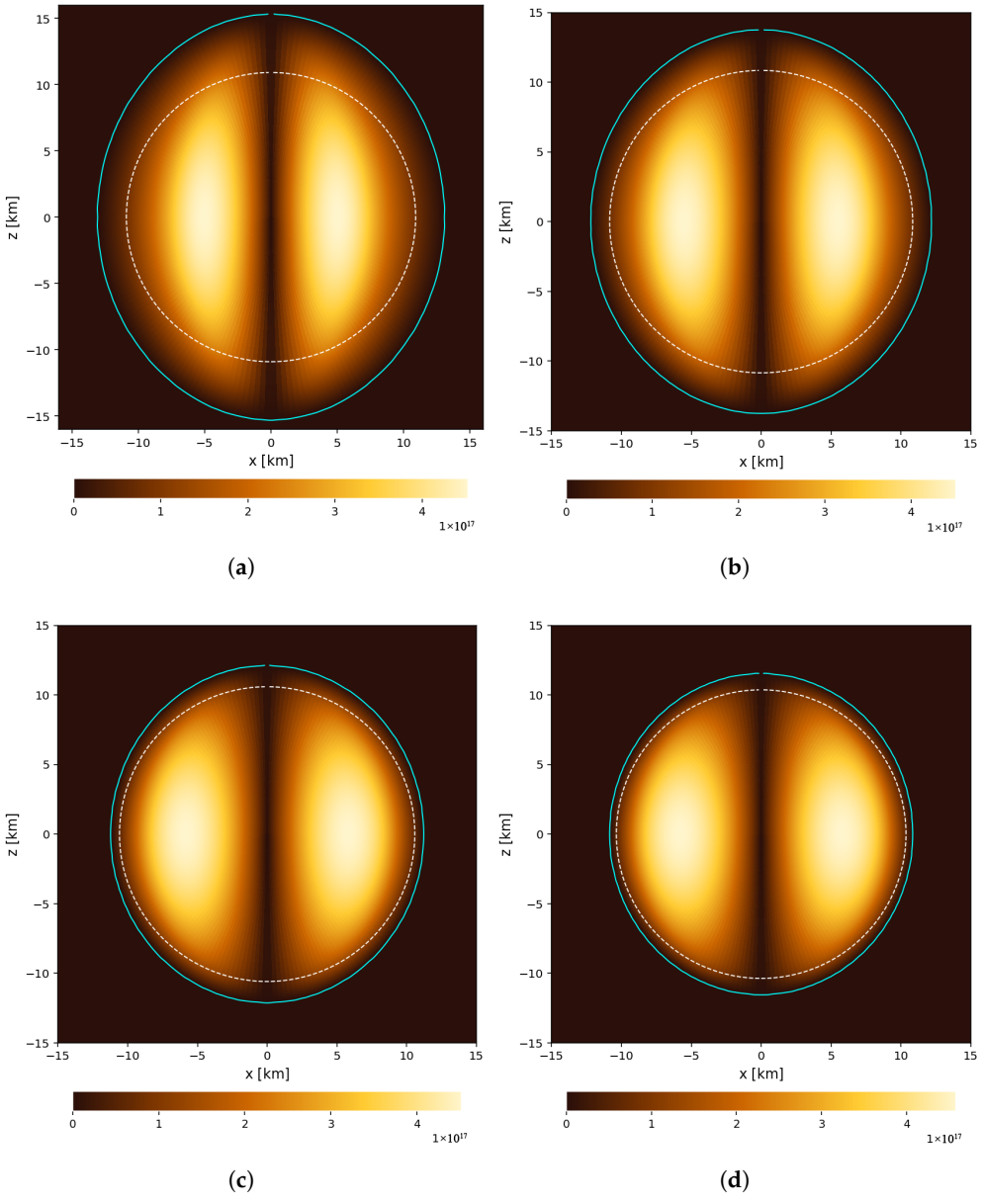

Figure 3. Meridional cross-sections of NSs with a purely toroidal magnetic field at four different gravitational masses: (**a**) 1.2 $M_{\odot}$, (**b**) 1.4 $M_{\odot}$, (**c**) 1.8 $M_{\odot}$, and (**d**) 2.0 $M_{\odot}$. The color map shows isocontours of the magnetic field strength ($|B|$) in Gauss. Solid cyan lines mark the stellar surfaces of the magnetized configurations, while dashed white lines indicate the corresponding unmagnetized reference stars of the same mass. All models share the same maximum magnetic field strength, $B_{\max} = 4.5 \times 10^{17}$ G.

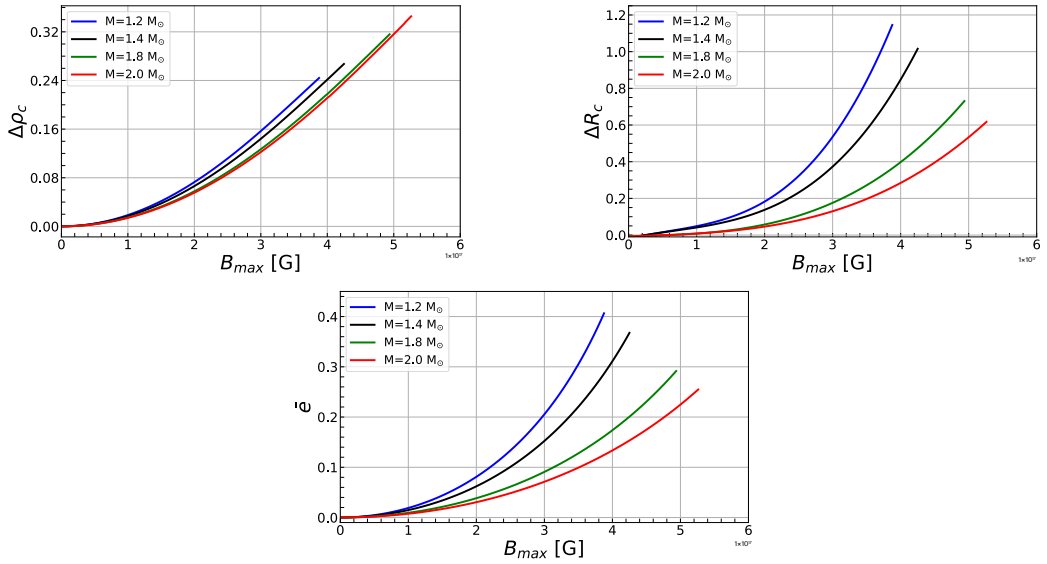

Figure 4. Variation of central density (**top-left**), circumferential radius (**top-right**), and mean deformation (**bottom**) relative to their non-magnetized counterparts, shown along equilibrium sequences at fixed gravitational mass for a purely toroidal magnetic field configuration.

4.2. Purely Poloidal Magnetic Field Configuration

In this section, we present equilibrium models constructed with a purely poloidal magnetic field, maintaining the same maximum field strength of $B_{\rm max} = 4.5 \times 10^{17}$ G. The global physical properties for this configuration are summarized in Table 2. As in the toroidal case, increasing the gravitational mass from 1.2 $M_\odot$ to 2.0 $M_\odot$ leads to a rise in central density (from 4.454 to 6.528 $\times 10^{14}$ g/cm^3), indicating that more massive stars are more compact. This trend is reflected in the decreasing equatorial radii (11.949, 11.597, 10.990, and 10.670 km) and circumferential radii (13.864, 13.825, 13.862, and 13.874 km) for the 1.2, 1.4, 1.8, and 2.0 $M_\odot$ models, respectively. As expected, the baryonic mass of each model exceeds its gravitational mass, reflecting the contribution of gravitational binding energy.

Table 2. Global physical quantities of the equilibrium models with maximum magnetic field strength in the purely poloidal case ($B_{\rm max} = 4.5 \times 10^{17}$ G). Here, ρ_c denotes the central baryon density, M the gravitational mass, m_b the baryonic mass, r_e the equatorial radius, r_p the polar radius, $R_{\rm circ}$ the circumferential radius, $\bar{e}$ the deformation parameter, Φ the magnetic flux.

M ($M_\odot$)	ρ_c (10^{14} g/cm^3)	m_b ($M_\odot$)	r_e (km)	r_p/r_e	$R_{\rm circ}$ (km)	$\bar{e}$ (10^{-1})	Φ (10^{21} Wb)
1.2	4.454	1.321	11.949	0.742	13.864	2.365	6.047
1.4	5.030	1.571	11.597	0.804	13.825	1.868	6.474
1.8	5.989	2.100	10.990	0.880	13.862	1.190	7.196
2.0	6.528	2.383	10.670	0.907	13.874	0.949	7.505

In this case, the magnetic pressure is strongest at the poles and along the equator, compressing the star along its symmetry axis and causing it to bulge outward at the equator. This results in an oblate shape. The polar-to-equatorial radius ratio (r_p/r_e) quantitatively confirms this, being less than unity for all models, with values of 0.742, 0.804, 0.880, and 0.907 for increasing masses. Consequently, the deformation parameter $\bar{e}$ is positive. As in the toroidal case, the magnitude of the deformation depends on mass: the 1.2 $M_\odot$ star is the most deformed ($\bar{e} = 2.365 \times 10^{-1}$), decreasing to $\bar{e} = 1.868 \times 10^{-1}$ for the 1.4 $M_\odot$ model and $\bar{e} = 1.190 \times 10^{-1}$ for the 1.8 $M_\odot$ model. The more gravitationally bound 2.0 $M_\odot$ star is the closest to spherical, with the smallest deformation of $\bar{e} = 0.949 \times 10^{-1}$.

The structure of the magnetic field and the resulting stellar deformation are illustrated in Figure 5. The figure highlights the characteristic dipole-like topology of a poloidal field. Unlike the toroidal configuration, the field is strongest at the stellar center and extends well into the exterior, a crucial feature for astrophysical phenomena such as pulsar emission. The oblate deformation is evident from the stellar surface (solid cyan line), which is compressed at the poles and extended at the equator. This visual evidence is consistent with the trends in the r_p/r_e ratio and the deformation parameter $\bar{e}$ reported in Table 2. The deformation is most pronounced in the 1.2 $M_\odot$ model (panel a) and progressively diminishes with increasing mass.

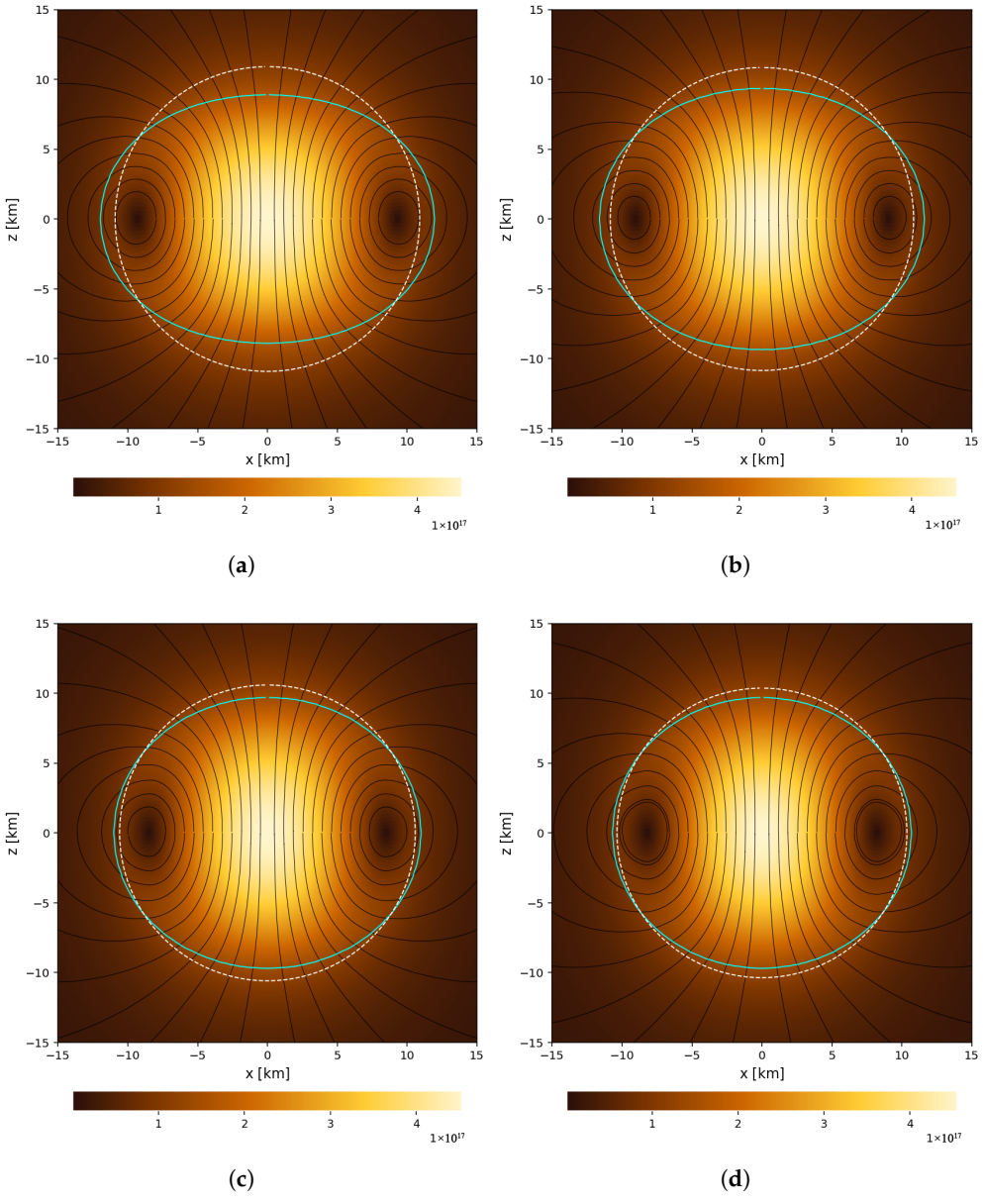

Figure 5. Meridional cross-sections of NSs with a purely poloidal magnetic field at four different gravitational masses: (**a**) 1.2 $M_\odot$, (**b**) 1.4 $M_\odot$, (**c**) 1.8 $M_\odot$, and (**d**) 2.0 $M_\odot$. The color map shows isocontours of the magnetic field strength ($|B|$) in Gauss. Solid cyan lines mark the stellar surfaces of the magnetized configurations, while dashed white lines indicate the corresponding unmagnetized reference stars of the same mass. All models share the same maximum magnetic field strength, $B_{\max} = 4.5 \times 10^{17}$ G.

As in the purely toroidal case, we also construct sequences of models at fixed gravitational mass while varying the magnetic field strength. Figure 6 illustrates the variation of

global quantities relative to their non-magnetized counterparts along equilibrium sequences at fixed mass. The plots show the relative changes in central density ($\Delta\rho_c$), circumferential radius ($\Delta R_{\rm circ}$), and mean deformation ($\bar{e}$) as functions of the maximum magnetic field strength, $B_{\rm max}$.

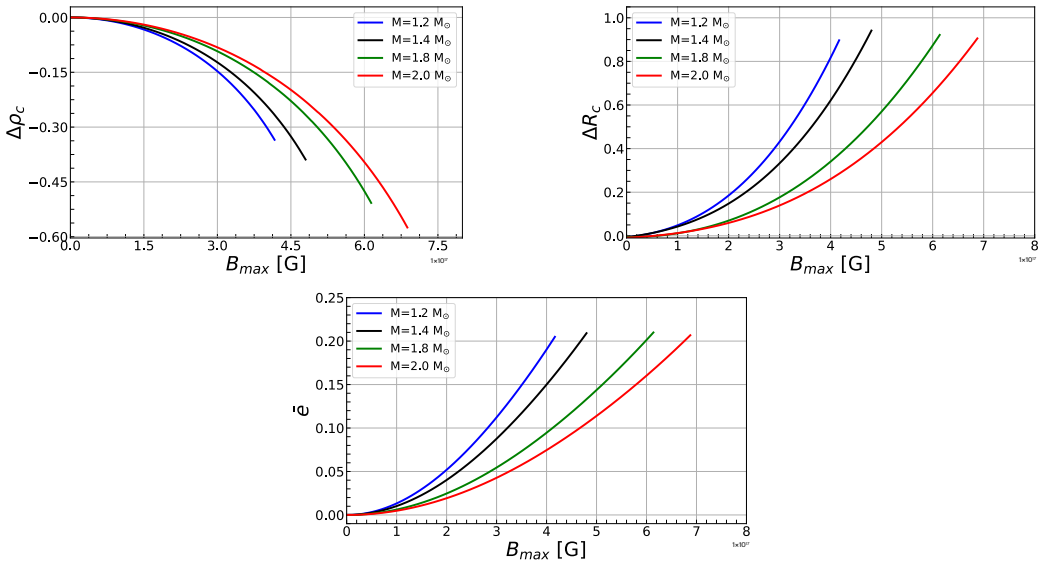

Figure 6. Variation of central density (**top-left**), circumferential radius (**top-right**), and mean deformation (**bottom**) relative to their non-magnetized counterparts, shown along equilibrium sequences at fixed gravitational mass for a purely poloidal magnetic field configuration.

The top-left panel reveals a behavior opposite to that of the toroidal configuration: for a given gravitational mass, the central density decreases as the magnetic field strength increases. This occurs because the Lorentz force in a poloidal geometry is dominated by an outward-pointing magnetic pressure gradient, which provides additional support against gravity throughout the star, including the core. Because the magnetic field itself supports a fraction of the stellar weight, the total fluid pressure required to balance gravity is reduced, preventing extreme compression of the core. To maintain hydrostatic equilibrium against gravity, less matter pressure is required, and therefore a lower central density suffices. This reduction in central density is accompanied by an overall expansion of the star, as shown in the top-right panel, where the circumferential radius increases with $B_{\rm max}$. The bottom panel quantifies the growth of the oblate deformation ($\bar{e}$), which is positive and increases non-linearly with field strength. A unifying theme emerges across all three plots, consistent with the toroidal case: the structural impact of the magnetic field is most pronounced in lower-mass stars. The 1.2 $M_\odot$ model (blue line) exhibits the largest decrease in density, the greatest expansion in radius, and the strongest deformation for any given field strength. This confirms that less gravitationally bound stars are more susceptible to reshaping by magnetic fields.

5. Astrophysical Implications

The equilibrium models presented in the previous sections demonstrate that internal magnetic fields of order 10^{17} G induce significant macroscopic deformations in NSs. Unlike the perturbative deformations caused by elastic crustal strains, which are typically limited to ellipticities of $\epsilon \sim 10^{-6}$, the magnetic deformations calculated here reach values of $|\bar{e}| \sim 10^{-1}$. These "giant" deformations have immediate and distinguishable consequences for two primary channels of multimessenger astronomy: continuous gravitational wave emission and X-ray pulse profile modeling.

5.1. Continuous Gravitational Waves from Toroidal Fields

Our results for purely toroidal magnetic fields (Table 1) indicate a prolate stellar shape, with deformation parameters ranging from $\bar{e} \approx -0.18$ for a 2.0 $M_\odot$ star to $\bar{e} \approx -0.67$ for a 1.2 $M_\odot$ star. This prolate geometry is dynamically significant because it influences the evolution of the star's orientation. A rotating prolate body is unstable to viscous dissipation if it spins about its symmetry axis; instead, it tends to evolve toward an orthogonal rotator configuration, where the spin axis is perpendicular to the magnetic symmetry axis [77]. This orthogonal configuration is the optimal geometry for the emission of continuous gravitational waves (CGWs). The characteristic strain amplitude h_0 of a CGW signal from a star with ellipticity $\epsilon \approx |\bar{e}|$, rotating at frequency f and located at distance d, is given by the quadrupole formula:

$$h_0 = \frac{4\pi^2 G}{c^4} \frac{I_{zz}|\bar{e}|f^2}{d}. \tag{21}$$

In this formulation, we identify the mean deformation parameter with the quadrupole ellipticity, $\epsilon \approx |\bar{e}|$. This approximation is reasonable for the axisymmetric, ellipsoidal mass distributions computed in Section 4, where the deviation from sphericity is driven by magnetic stress rather than rotational flattening [78]. Consequently, current observational upper limits on ellipticity derived from CGW searches—such as those targeting the Crab or Vela pulsars—could be used to place indirect constraints on internal magnetic field strengths by bounding the maximum allowable $\bar{e}$.

For a canonical NS with $I_{zz} \approx 10^{38}$ kg m^2 and the deformation $|\bar{e}| \approx 0.1$ found in our models, the potential GW strain is several orders of magnitude larger than that expected from crustal mountains. The large deformation values obtained here should be interpreted as extreme upper limits. In realistic astrophysical scenarios, such configurations would likely undergo rapid gravitational-wave-driven evolution, limiting their long-term stability. Consequently, these states cannot represent long-term stable astrophysical equilibria. Such extreme deformations would likely only exist transiently, for instance, in the immediate aftermath of a binary NS merger or during a magnetar's birth phase before the star rapidly radiates away this energy and relaxes into a less deformed state [79]. Quantitatively, for an NS with a deformation of $|\bar{e}| \sim 0.1$, the gravitational-wave luminosity scales as $L_{GW} \propto \epsilon^2 f^6$. For the extreme configurations reported in Tables 1 and 2, the resulting spin-down timescale ($\tau = f/\dot{f}$) would be on the order of seconds to minutes. This confirms that while such equilibrium states are mathematically valid solutions to the XNS equations, they represent a transient evolutionary phase rather than the long-term population of steady-state pulsars. For a hypothetical newborn magnetar rotating at 1 kHz at the distance of the Virgo cluster (20 Mpc), such a deformation would yield a strain detectable by current interferometers such as LIGO, Virgo, and KAGRA. However, the energy loss associated with such a massive quadrupole moment would be catastrophic, leading to a spin-down timescale of only seconds to minutes [79]. Therefore, while stable high-field toroidal configurations are potent GW sources, they are more likely to manifest as transient signals following binary mergers or supernovae (e.g., magnetar birth) rather than as long-lived continuous sources, unless the rotation rate is significantly low ($f < 10$ Hz). For these slowly rotating, highly deformed objects, third-generation detectors such as the Einstein Telescope and Cosmic Explorer will be required to probe the population [80,81].

5.2. Systematic Bias in X-Ray Radius Measurements

Conversely, our models with purely poloidal fields (Table 2) exhibit oblate deformations with $\bar{e}$ values between 0.09 and 0.24. This deformation mimics the flattening caused by rapid rotation but arises entirely from internal magnetic pressure. Our results demon-

strate that a strong internal poloidal field can induce oblateness comparable to that of a millisecond pulsar, even in a slowly rotating star. For a 1.4 $M_\odot$ model, the poloidal field produces a deformation of $\bar{e} \approx 0.187$. If such a star were analyzed under the standard assumption of rotational flattening, the "excess" magnetic oblateness would not be incorporated into the ray-tracing background metric, introducing a systematic bias in the inferred equatorial radius.

This has critical implications for radius measurements via X-ray Pulse Profile Modeling (PPM), the primary technique employed by the NICER mission [39,66,82]. PPM infers stellar mass and radius by analyzing relativistic light bending and Doppler boosting of thermal emission from surface hot spots. Current inference pipelines typically assume that the NS shape is determined exclusively by its rotation rate, often adopting the Oblate Schwarzschild approximation [83,84]. Given that NICER aims for radius constraints at the $\sim$5% level to distinguish between nuclear EoSs, neglecting magnetic deformation in magnetars or central compact objects could lead to erroneous conclusions regarding the stiffness of dense matter. By mapping the relationship between magnetic field topology and the deformation parameter $\bar{e}$, our results provide a framework for incorporating magnetic priors into future GW searches and X-ray parameter estimation pipelines.

The theoretical possibility of a 2.6 $M_\odot$ magnetized NS must be viewed alongside its observational rarity. Highly magnetized stars with $|\bar{e}| \sim 10^{-1}$ would undergo rapid spin-down due to gravitational-wave emission, likely having lifetimes far shorter than traditional pulsars. Consequently, while our models provide a candidate for mass-gap objects like GW190814, such stars are likely transient phenomena (e.g., newborn magnetars) rather than stable, long-lived components of the galactic population. This 'temporary' support for high masses may explain the scarcity of such detections and the apparent discrepancy with the more conservative tidal limits derived from older, less magnetized binary systems like GW170817.

6. Conclusions

In this work, we conducted a comprehensive study of the structural deformations induced by strong magnetic fields in neutron stars (NSs), employing the Density-Dependent Meson-Exchange (DDME2) equation of state (EoS). By combining spherical solutions of the Tolman–Oppenheimer–Volkoff (TOV) equations with self-consistent axisymmetric equilibrium models computed using the `XNS` code, we mapped the interplay between internal magnetic field topology, field strength, and macroscopic stellar observables.

Our analysis of the spherical models demonstrates that density-dependent magnetic fields significantly stiffen the EoS. For extreme dipole moments corresponding to central fields of order 10^{17} G, there is an increase in the maximum stable mass of approximately 8% and an expansion of the canonical 1.4 $M_\odot$ radius of about 6%. Consequently, the tidal deformability Λ rises substantially, indicating that magnetic effects must be carefully disentangled from nuclear physics uncertainties when interpreting gravitational-wave signals from binary mergers. We emphasize that these spherical solutions represent an upper-bound approximation. A fully self-consistent treatment of metric distortions requires advanced spectral solvers such as the LORENE library, which we identify as a subject for future investigation. Nevertheless, our present results provide valuable bounds on the mass–radius enhancement driven purely by magnetic modifications of the dense matter phase space.

The axisymmetric models reveal the expected variation in stellar response to strong magnetic fields across different masses. For a fixed field strength of 4.5×10^{17} G, lower-mass stars exhibit the largest changes in central density, radius, and other global quantities compared to their non-magnetized counterparts, reflecting their weaker gravitational bind-

ing. In contrast, higher-mass stars display only modest variations under the same magnetic conditions. This trend is present in both toroidal and poloidal configurations and is further supported by the fixed-mass sequences, where the influence of the field decreases steadily with increasing mass. Overall, the results confirm that magnetic effects are strongest in lower-mass NSs, while more massive stars remain relatively stable. These "giant" deformations have profound implications for multi-messenger astrophysics. The prolate shapes associated with toroidal fields suggest that highly magnetized NSs may be potent sources of continuous gravitational waves (GWs). However, given the immense energy loss rates implied by ellipticities of order 10^{-1}, such signals are likely to be transient or require the star to be a slow rotator detectable only by third-generation interferometers such as the Einstein Telescope. Conversely, the oblate shapes driven by poloidal fields present a critical systematic challenge for X-ray pulse profile modeling. The magnetic oblateness we have quantified ($\bar{e}\sim 0.2$) mimics rotational flattening but occurs independently of spin frequency. Neglecting this effect in the analysis of data from missions like NICER could lead to biased radius measurements and erroneous constraints on the dense matter EoS.

Beyond confirming earlier findings on magnetic stiffening and deformation, our work provides an independent verification by employing a density-dependent magnetic field profile together with the realistic DDME2 nuclear equation of state. This dual framework—combining spherical TOV baselines with axisymmetric XNS simulations—strengthens confidence in prior results while modernizing them in the context of multimessenger astronomy. In particular, the explicit mapping between field strength, topology, and stellar mass highlights how magnetic deformations may bias NICER radius measurements and gravitational-wave interpretations, underscoring the importance of incorporating magnetization effects into current observational analyses.

Future work will focus on assessing the dynamical stability of these highly deformed configurations through full General Relativistic Magnetohydrodynamic (GRMHD) evolutions. We also plan to incorporate LORENE-based initial data to rigorously model the stability of such configurations. Furthermore, extending this framework to include realistic microphysics—such as superfluidity and superconductivity—will be essential for refining estimates of magnetic damping timescales and the longevity of gravitational-wave sources.

Author Contributions: Conceptualization, H.C., I.A.R., P.T. and T.K.J.; methodology, H.C. and I.A.R.; software, H.C. and I.A.R.; formal analysis, H.C. and I.A.R.; writing original draft preparation, H.C., I.A.R. and C.B.; writing review and editing, H.C., I.A.R. and C.B.; supervision, O.L., M.D. and R.N. All authors have read and agreed to the published version of the manuscript.

Funding: This work has been done as a part of the Project INCT-Física Nuclear e Aplicações, under No. 408419/2024-5. It is also supported by Conselho Nacional de Desenvolvimento Científico e Tecnológico (CNPq) under Grants No. 444797/2024-6 (O.L., M.D., R.N), No. 307255/2023-9 (O.L.), No. 301779/2025-2 (M.D.), No. 401565/2023-8 (Universal—O.L., M.D.), No. 409736/2025-2 (Universal—O.L., M.D.), and Fundação de Amparo à Pesquisa do Estado de São Paulo (FAPESP) under Thematic Project No. 2024/17816-8 (O.L., M.D.), and Project No. 2025/06216-2 (C.B.). P. Thakur is supported by the National Research Foundation of Korea (NRF) grant funded by the Korea government (MSIT) (No. RS-2024-00457037). This work was supported (in part) by the Yonsei University Research Fund (Yonsei University Frontier Fellowship for Postdoctoral Researchers) of 2025.

Data Availability Statement: The data that support the findings of this article are not publicly available. The data are available from the authors upon reasonable request.

Acknowledgments: I.A.R. acknowledges support from the Alexander von Humboldt Foundation.

Conflicts of Interest: The authors declare no conflicts of interest.

References

1. Lai, D.; Shapiro, S.L. Cold Equation of State in a Strong Magnetic Field: Effects of Inverse beta-Decay. *Astrophys. J.* **1991**, *383*, 745–751. [CrossRef]
2. Broderick, A.; Prakash, M.; Lattimer, J.M. The Equation of State of Neutron Star Matter in Strong Magnetic Fields. *Astrophys. J.* **2000**, *537*, 351–367. [CrossRef]
3. Chatterjee, D.; Elghozi, T.; Novak, J.; Oertel, M. Consistent neutron star models with magnetic field dependent equations of state. *Mon. Not. R. Astron. Soc.* **2015**, *447*, 3785–3796. [CrossRef]
4. Bocquet, M.; Bonazzola, S.; Gourgoulhon, E.; Novak, J. Rotating neutron star models with magnetic field. *Astron. Astrophys.* **1995**, *301*, 757.
5. Cardall, C.Y.; Prakash, M.; Lattimer, J.M. Effects of Strong Magnetic Fields on Neutron Star Structure. *Astrophys. J.* **2001**, *554*, 322–339. [CrossRef] [PubMed]
6. Ciolfi, R.; Ferrari, V.; Gualtieri, L. Structure and deformations of strongly magnetized neutron stars with twisted-torus configurations. *Mon. Not. R. Astron. Soc.* **2010**, *406*, 2540–2548. [CrossRef]
7. Frieben, J.; Rezzolla, L. Equilibrium models of relativistic stars with a toroidal magnetic field. *Mon. Not. R. Astron. Soc.* **2012**, *427*, 3406–3426. [CrossRef]
8. Pili, A.G.; Bucciantini, N.; Del Zanna, L. Axisymmetric equilibrium models for magnetized neutron stars in General Relativity under the Conformally Flat Condition. *Mon. Not. R. Astron. Soc.* **2014**, *439*, 3541–3563. [CrossRef]
9. Bonazzola, S.; Gourgoulhon, E.; Salgado, M.; Marck, J.A. Axisymmetric rotating relativistic bodies: A new numerical approach for 'exact' solutions. *Astron. Astrophys.* **1993**, *278*, 421–443.
10. Pili, A.G.; Bucciantini, N.; Del Zanna, L. General relativistic models for rotating magnetized neutron stars in conformally flat space–time. *Mon. Not. R. Astron. Soc.* **2017**, *470*, 2469–2493. [CrossRef]
11. Dexheimer, V.; Franzon, B.; Gomes, R.O.; Farias, R.L.S.; Avancini, S.S.; Schramm, S. What is the magnetic field distribution for the equation of state of magnetized neutron stars? *Phys. Lett. B* **2017**, *773*, 487–491. [CrossRef]
12. Makishima, K.; Enoto, T.; Hiraga, J.S.; Nakano, T.; Nakazawa, K.; Sakurai, S.; Sasano, M.; Murakami, H. Possible Evidence for Free Precession of a Strongly Magnetized Neutron Star in the Magnetar 4U 0142+61. *Phys. Rev. Lett.* **2014**, *112*, 171102. [CrossRef] [PubMed]
13. Dall'Osso, S.; Stella, L.; Palomba, C. Neutron star bulk viscosity, 'spin-flip' and GW emission of newly born magnetars. *Mon. Not. R. Astron. Soc.* **2018**, *480*, 1353–1362. [CrossRef]
14. Lander, S.K.; Jones, D.I. Neutron-star spindown and magnetic inclination-angle evolution. *Mon. Not. R. Astron. Soc.* **2018**, *481*, 4169–4193. [CrossRef]
15. Kuzur, D.; Mallick, R. Frame-dragging effects in obliquely rotating magnetars. *J. Astrophys. Astron.* **2021**, *42*, 87. [CrossRef]
16. Price, D.; Rosswog, S. Producing ultra-strong magnetic fields in neutron star mergers. *Science* **2006**, *312*, 719–722. [CrossRef]
17. Giacomazzo, B.; Zrake, J.; Duffell, P.; MacFadyen, A.I.; Perna, R. Producing Magnetar Magnetic Fields in the Merger of Binary Neutron Stars. *Astrophys. J.* **2015**, *809*, 39. [CrossRef]
18. Most, E.R.; Papenfort, L.J.; Rezzolla, L. Beyond second-order convergence in simulations of magnetized binary neutron stars with realistic microphysics. *Mon. Not. R. Astron. Soc.* **2019**, *490*, 3588–3600. [CrossRef]
19. Raynaud, R.; Guilet, J.; Janka, H.T.; Gastine, T. Magnetar formation through a convective dynamo in protoneutron stars. *Sci. Adv.* **2020**, *6*, eaay2732. [CrossRef]
20. Chakrabarty, S.; Bandyopadhyay, D.; Pal, S. Dense Nuclear Matter in a Strong Magnetic Field. *Phys. Rev. Lett.* **1997**, *78*, 2898–2901. [CrossRef]
21. Rabhi, A.; Providência, C.; Providência, J.D. Stellar matter with a strong magnetic field within density-dependent relativistic models. *J. Phys. G Nucl. Part. Phys.* **2008**, *35*, 125201. [CrossRef]
22. Mallick, R.; Schramm, S. Deformation of a magnetized neutron star. *Phys. Rev. C* **2014**, *89*, 045805. [CrossRef]
23. Bandyopadhyay, D.; Chakrabarty, S.; Pal, S. Quantizing Magnetic Field and Quark-Hadron Phase Transition in a Neutron Star. *Phys. Rev. Lett.* **1997**, *79*, 2176–2179. [CrossRef]
24. Aguirre, R.M. Vacuum effects on the properties of nuclear matter under an external magnetic field. *Phys. Rev. C* **2019**, *100*, 065203. [CrossRef]
25. Gomes, R.O.; Franzon, B.; Dexheimer, V.; Schramm, S. Many-body forces in magnetic neutron stars. *Astrophys. J.* **2017**, *850*, 20. [CrossRef]
26. Dexheimer, V.; Negreiros, R.; Schramm, S. Hybrid Stars in a Strong Magnetic Field. *Eur. Phys. J. A* **2012**, *48*, 189. [CrossRef]
27. Felipe, R.G.; Martinez, A.P.; Rojas, H.P.; Orsaria, M. Magnetized strange quark matter and magnetized strange quark stars. *Phys. Rev. C* **2008**, *77*, 015807. [CrossRef]
28. Paulucci, L.; Ferrer, E.J.; de la Incera, V.; Horvath, J.E. Magnetic Color-flavor-locked Stars. *Proc. Int. Astron. Union* **2013**, *291*, 465–467. [CrossRef]

29. Casali, R.H.; Castro, L.B.; Menezes, D.P. Hadronic and hybrid stars subject to density dependent magnetic fields. *Phys. Rev. C* **2014**, *89*, 015805. [CrossRef]
30. Tolman, R.C. Static Solutions of Einstein's Field Equations for Spheres of Fluid. *Phys. Rev.* **1939**, *55*, 364–373. [CrossRef]
31. Oppenheimer, J.R.; Volkoff, G.M. On Massive Neutron Cores. *Phys. Rev.* **1939**, *55*, 374–381. [CrossRef]
32. Kiuchi, K.; Yoshida, S. Relativistic stars with purely toroidal magnetic fields. *Phys. Rev. D* **2008**, *78*, 044045. [CrossRef]
33. Lalazissis, G.A.; Nikšić, T.; Vretenar, D.; Ring, P. New relativistic mean-field interaction with density-dependent meson-nucleon couplings. *Phys. Rev. C* **2005**, *71*, 024312. [CrossRef]
34. Abbott, B.P.; Abbott, R.; Abbott, T.D.; Acernese, F.; Ackley, K.; Adams, C.; Adams, T.; Addesso, P.; Adhikari, R.X.; Adya, V.B.; et al. GW170817: Measurements of neutron star radii and equation of state. *Phys. Rev. Lett.* **2018**, *121*, 161101. [CrossRef] [PubMed]
35. Abbott, B.P.; Abbott, R.; Abbott, T.D.; Acernese, F.; Ackley, K.; Adams, C.; Adams, T.; Addesso, P.; Adhikari, R.X.; Adya, V.B.; et al. GW170817: Observation of Gravitational Waves from a Binary Neutron Star Inspiral. *Phys. Rev. Lett.* **2017**, *119*, 161101. [CrossRef]
36. Biswas, B.; Nandi, R.; Char, P.; Bose, S.; Stergioulas, N. GW190814: On the properties of the secondary component of the binary. *arXiv* **2020**, arXiv:2010.02090. [CrossRef]
37. Abbott, R.; Abbott, T.D.; Abraham, S.; Acernese, F.; Ackley, K.; Adams, C.; Adhikari, R.X.; Adya, V.B.; Affeldt, C.; Agathos, M.; et al. GW190814: Gravitational Waves from the Coalescence of a 23 Solar Mass Black Hole with a 2.6 Solar Mass Compact Object. *Astrophys. J. Lett.* **2020**, *896*, L44. [CrossRef]
38. Riley, T.E.; Watts, A.L.; Bogdanov, S.; Ray, P.S.; Ludlam, R.M.; Guillot, S.; Arzoumanian, Z.; Baker, C.L.; Bilous, A.V.; Chakrabarty, D.; et al. A *NICER* View of PSR J0030+0451: Millisecond Pulsar Parameter Estimation. *Astrophys. J. Lett.* **2019**, *887*, L21. [CrossRef]
39. Miller, M.C.; Lamb, F.K.; Dittmann, A.J.; Bogdanov, S.; Arzoumanian, Z.; Gendreau, K.C.; Guillot, S.; Harding, A.K.; Ho, W.C.G.; Lattimer, J.M.; et al. PSR J0030+0451 Mass and Radius from NICER Data and Implications for the Properties of Neutron Star Matter. *Astrophys. J. Lett.* **2019**, *887*, L24. [CrossRef]
40. Adhikari, P.; Ammon, M.; Avancini, S.S.; Ayala, A.; Bandyopadhyay, A.; Blaschke, D.; Braghin, F.L.; Buividovich, P.; Cardoso, R.P.; Cartwright, C.; et al. Strongly interacting matter in extreme magnetic fields. *Prog. Part. Nucl. Phys.* **2026**, *146*, 104199. [CrossRef]
41. Gomes, R.O.; Dexheimer, V.; Schramm, S.; Vasconcellos, C. Many-body forces in the equation of state of hyperonic matter. *Astrophys. J.* **2015**, *808*, 8. [CrossRef]
42. Gomes, R.O.; Dexheimer, V.; Han, S.; Schramm, S. Can magnetic fields (de)stabilize twin stars? *Mon. Not. R. Astron. Soc.* **2019**, *485*, 4873–4877. [CrossRef]
43. Gomes, R.O.; Pais, H.; Dexheimer, V.; Providência, C.; Schramm, S. Limiting magnetic field for minimal deformation of a magnetized neutron star. *Astron. Astrophys.* **2019**, *627*, A61. [CrossRef]
44. Goldreich, P.; Reisenegger, A. Magnetic field decay in isolated neutron stars. *Astrophys. J.* **1992**, *395*, 250–258. [CrossRef] [PubMed]
45. Giacomazzo, B.; Perna, R. Formation of Stable Magnetars from Binary Neutron Star Mergers. *Astrophys. J. Lett.* **2013**, *771*, L26. [CrossRef]
46. Dexheimer, V.; Menezes, D.P.; Strickland, M. The influence of strong magnetic fields on proto-quark stars. *J. Phys. G Nucl. Part. Phys.* **2013**, *41*, 015203. [CrossRef]
47. Haskell, B.; Samuelsson, L.; Glampedakis, K.; Andersson, N. Modelling magnetically deformed neutron stars. *Mon. Not. R. Astron. Soc.* **2008**, *385*, 531–542. [CrossRef]
48. Harding, A.K.; Lai, D. Physics of Strongly Magnetized Neutron Stars. *Rep. Prog. Phys.* **2006**, *69*, 2631–2708. [CrossRef]
49. Rather, I.A.; Rahaman, U.; Dexheimer, V.; Usmani, A.A.; Patra, S.K. Heavy Magnetic Neutron Stars. *Astrophys. J.* **2021**, *917*, 46. [CrossRef]
50. Rather, I.A.; Rather, A.A.; Dexheimer, V.; Lopes, I.; Usmani, A.A.; Patra, S.K. Magnetic-field Induced Deformation in Hybrid Stars. *Astrophys. J.* **2023**, *943*, 52. [CrossRef]
51. Brockmann, R.; Toki, H. Relativistic density-dependent Hartree approach for finite nuclei. *Phys. Rev. Lett.* **1992**, *68*, 3408–3411. [CrossRef] [PubMed]
52. Huang, K.; Hu, J.; Zhang, Y.; Shen, H. The Possibility of the Secondary Object in GW190814 as a Neutron Star. *Astrophys. J.* **2020**, *904*, 39. [CrossRef]
53. Typel, S.; Wolter, H. Relativistic mean field calculations with density-dependent meson-nucleon coupling. *Nucl. Phys. A* **1999**, *656*, 331–364. [CrossRef]
54. Rather, I.A.; Usmani, A.A.; Patra, S.K. Hadron–quark phase transition in the context of GW190814. *J. Phys. G* **2021**, *48*, 085201. [CrossRef]
55. Rather, I.A. Relativistic Mean Field Study of Neutron Stars and Hyperon Stars. Ph.D. Thesis, Department of Physics, Aligarh Muslim University, Aligarh, India, 2021. Available online: http://arxiv.org/abs/2206.02202 (accessed on 23 April 2026).
56. Huang, X.G.; Huang, M.; Rischke, D.H.; Sedrakian, A. Anisotropic hydrodynamics, bulk viscosities, and *r*-modes of strange quark stars with strong magnetic fields. *Phys. Rev. D* **2010**, *81*, 045015. [CrossRef]

57. Khalilov, V.R. Macroscopic effects in cold magnetized nucleons and electrons with anomalous magnetic moments. *Phys. Rev. D* **2002**, *65*, 056001. [CrossRef]
58. Potekhin, A.Y.; Yakovlev, D.G. Comment on "Equation of state of a dense and magnetized fermion system". *Phys. Rev. C* **2012**, *85*, 039801. [CrossRef]
59. Bucciantini, N.; Del Zanna, L. General relativistic magnetohydrodynamics in axisymmetric dynamical spacetimes: The X-ECHO code. *Astron. Astrophys.* **2011**, *528*, A101. [CrossRef]
60. Cordero-Carrion, I.; Cerda-Duran, P.; Dimmelmeier, H.; Jaramillo, J.L.; Novak, J.; Gourgoulhon, E. Improved constrained scheme for the Einstein equations: An Approach to the uniqueness issue. *Phys. Rev. D* **2009**, *79*, 024017. [CrossRef]
61. Ciolfi, R.; Ferrari, V.; Gualtieri, L.; Pons, J.A. Relativistic models of magnetars: The twisted torus magnetic field configuration. *Mon. Not. R. Astron. Soc.* **2009**, *397*, 913–924. [CrossRef]
62. Wu, F.; Wu, C.; Ren, Z. Neutron stars including the effects of chaotic magnetic fields and anomalous magnetic moments. *Chin. Phys. C* **2017**, *41*, 045102. [CrossRef]
63. Lopes, L.L.; Menezes, D. On Magnetized Neutron Stars. *J. Cosmol. Astropart. Phys.* **2015**, *2015*, 002. [CrossRef]
64. Rather, I.A.; Dexheimer, V.; Lopes, I. Phase Transitions under Strong Magnetic Fields in Neutron Star. *EPJ Web Conf.* **2023**, *290*, 03004. [CrossRef]
65. Alloy, M.D.; Menezes, D.P. Maxwell equation violation by density dependent magnetic fields in neutron stars. *Int. J. Mod. Phys. Conf. Ser.* **2017**, *45*, 1760031. [CrossRef]
66. Miller, M.C.; Lamb, F.K.; Dittmann, A.J.; Bogdanov, S.; Arzoumanian, Z.; Gendreau, K.C.; Guillot, S.; Ho, W.C.G.; Lattimer, J.M.; Loewenstein, M.; et al. The Radius of PSR J0740+6620 from NICER and XMM-Newton Data. *Astrophys. J. Lett.* **2021**, *918*, L28. [CrossRef]
67. Riley, T.E.; Watts, A.L.; Ray, P.S.; Bogdanov, S.; Guillot, S.; Morsink, S.M.; Bilous, A.V.; Arzoumanian, Z.; Choudhury, D.; Deneva, J.S.; et al. A NICER View of the Massive Pulsar PSR J0740+6620 Informed by Radio Timing and XMM-Newton Spectroscopy. *Astrophys. J. Lett.* **2021**, *918*, L27. [CrossRef]
68. Choudhury, D.; Salmi, T.; Vinciguerra, S.; Riley, T.E.; Kini, Y.; Watts, A.L.; Dorsman, B.; Bogdanov, S.; Guillot, S.; Ray, P.S.; et al. A NICER View of the Nearest and Brightest Millisecond Pulsar: PSR J0437-4715. *Astrophys. J. Lett.* **2024**, *971*, L20. [CrossRef]
69. Salmi, T.; Choudhury, D.; Kini, Y.; Riley, T.E.; Vinciguerra, S.; Watts, A.L.; Wolff, M.T.; Arzoumanian, Z.; Bogdanov, S.; Chakrabarty, D.; et al. The Radius of the High-mass Pulsar PSR J0740+6620 with 3.6 yr of NICER Data. *Astrophys. J.* **2024**, *974*, 294. [CrossRef]
70. Dittmann, A.J.; Miller, M.C.; Lamb, F.K.; Holt, I.M.; Chirenti, C.; Wolff, M.T.; Bogdanov, S.; Guillot, S.; Ho, W.C.G.; Morsink, S.M.; et al. A More Precise Measurement of the Radius of PSR J0740+6620 Using Updated NICER Data. *Astrophys. J.* **2024**, *974*, 295. [CrossRef]
71. Mauviard, L.; Guillot, S.; Salmi, T.; Choudhury, D.; Dorsman, B.; González-Caniulef, D.; Hoogkamer, M.; Huppenkothen, D.; Kazantsev, C.; Kini, Y.; et al. A NICER View of the 1.4 $M_{\odot}$ Edge-on Pulsar PSR J0614-3329. *Astrophys. J.* **2025**, *995*, 60. [CrossRef]
72. Hinderer, T.; Lackey, B.D.; Lang, R.N.; Read, J.S. Tidal deformability of neutron stars with realistic equations of state and their gravitational wave signatures in binary inspiral. *Phys. Rev. D* **2010**, *81*, 123016. [CrossRef]
73. Kumar, B.; Biswal, S.K.; Patra, S.K. Tidal deformability of neutron and hyperon stars within relativistic mean field equations of state. *Phys. Rev. C* **2017**, *95*, 015801. [CrossRef]
74. Gourgoulhon, E.; Grandclément, P.; Marck, J.A.; Novak, J.; Taniguchi, K. LORENE: Langage Objet pour la Relativité Numérique. Free Software Under GNU General Public License. Developed at LUTH, Observatoire de Paris. 2026. Available online: http://www.lorene.obspm.fr (accessed on 23 April 2026).
75. Braithwaite, J.; Spruit, H.C. A fossil origin for the magnetic field in A stars and white dwarfs. *Nature* **2004**, *431*, 819–821. [CrossRef]
76. Ciolfi, R.; Rezzolla, L. Poloidal-Field Instability in Magnetized Relativistic Stars. *Astrophys. J.* **2012**, *760*, 1. [CrossRef]
77. Cutler, C. Gravitational waves from neutron stars with large toroidal B fields. *Phys. Rev. D* **2002**, *66*, 084025. [CrossRef]
78. Gourgoulhon, E.; Bonazzola, S. Gravitational waves from isolated neutron stars. In Proceedings of the International Conference on Gravitational Waves: Sources and Detectors, Cascina, Italy, 19–23 March 1996. Available online: http://arxiv.org/abs/astro-ph/9605150 (accessed on 23 April 2026).
79. Stella, L.; Dall'Osso, S.; Israel, G.L.; Vecchio, A. Gravitational Radiation from Newborn Magnetars in the Virgo Cluster. *Astrophys. J.* **2005**, *634*, l165–l168. [CrossRef]
80. Punturo, M.; Abernathy, M.; Acernese, F.; Allen, B.; Andersson, N.; Arun, K.; Barone, F.; Barr, B.; Barsuglia, M.; Beker, M.; et al. The Einstein Telescope: A third-generation gravitational wave observatory. *Class. Quantum Gravity* **2010**, *27*, 194002. [CrossRef]
81. Abbott, B.P.; Abbott, R.; Abbott, T.D.; Abernathy, M.R.; Ackley, K.; Adams, C.; Addesso, P.; Adhikari, R.X.; Adya, V.B.; Affeldt, C.; et al. Exploring the Sensitivity of Next Generation Gravitational Wave Detectors. *Class. Quantum Gravity* **2017**, *34*, 044001. [CrossRef]
82. Hoogkamer, M.; Rutherford, N.; Huppenkothen, D.; Ricketts, B.; Watts, A.L.; Mendes, M.; Svensson, I.; Schwenk, A.; Kramer, M.; Hebeler, K.; et al. Equation-of-state-informed pulse profile modeling. *Phys. Rev. D* **2026**, *113*, 063049. [CrossRef]

83. Morsink, S.M.; Leahy, D.A.; Cadeau, C.; Braga, J. The Oblate Schwarzschild Approximation for Light Curves of Rapidly Rotating Neutron Stars. *Astrophys. J.* **2007**, *663*, 1244–1251. [CrossRef]
84. AlGendy, M.; Morsink, S.M. Universality of the Acceleration due to Gravity on the Surface of a Rapidly Rotating Neutron Star. *Astrophys. J.* **2014**, *791*, 78. [CrossRef]

Disclaimer/Publisher's Note: The statements, opinions and data contained in all publications are solely those of the individual author(s) and contributor(s) and not of MDPI and/or the editor(s). MDPI and/or the editor(s) disclaim responsibility for any injury to people or property resulting from any ideas, methods, instructions or products referred to in the content.